

Phase field crystal study of deformation and plasticity in nanocrystalline materials

Peter Stefanovic,¹ Mikko Haataja,² and Nikolas Provatas¹

¹*Department of Materials Science and Engineering and Brockhouse Institute for Materials Research, McMaster University, Hamilton, Ontario, Canada L8S-4L7*

²*Department of Mechanical and Aerospace Engineering, Princeton University, Olden Street, Princeton, New Jersey 08544, USA*
(Received 7 April 2009; published 13 October 2009)

We introduce a modified phase field crystal (MPFC) technique that self-consistently incorporates rapid strain relaxation alongside the usual plastic deformation and multiple crystal orientations featured by the traditional phase field crystal (PFC) technique. Our MPFC formalism can be used to study a host of important phase transformation phenomena in material processing that require rapid strain relaxation. We apply the MPFC model to study elastic and plastic deformations in nanocrystalline materials, focusing on the “reverse” Hall-Petch effect. Finally, we introduce a multigrid algorithm for efficient numerical simulations of the MPFC model.

DOI: [10.1103/PhysRevE.80.046107](https://doi.org/10.1103/PhysRevE.80.046107)

PACS number(s): 62.20.F-, 46.15.-x, 64.60.Cn, 73.63.Bd

I. INTRODUCTION

Understanding the evolution of microstructure and its interactions with defects enables us to predict the behavior of a material in practical applications. Even a basic uniaxial tensile test activates a wealth of processes inside a metal. When line defects—or dislocations—interact with grain and/or phase boundaries, the grains can change their shape and orientation, and voids appear. While these processes occur simultaneously, their length scales and time scales vary across several orders of magnitude.

Processes on mesoscopic length scales ($\sim \mu\text{m}$), such as deformation and microstructure evolution, have been traditionally modeled by phase field models coupled with elasticity, dislocations, or concentration fields [1–3]. The phase field method ascribes spatially uniform values for the so-called order parameter(s) (OP) within a given phase, while the phase or grain boundaries can be identified with regions where the OPs undergo rapid variations. Within the classical phase field approach, the atomic scale details of interfaces and other defects are necessarily smeared out. Important processes on atomic length scales (nm), such as dislocation nucleation and motion, have been traditionally modeled using molecular-dynamics (MD) simulations. On the other hand, while MD simulations provide detailed information about atomistic processes, they are generally limited to time scales of nanoseconds (10^{-9} s) and relatively small sample sizes ($\sim 10^7$ atoms) [4]. As a consequence, only high stresses (GPa) and strain rates (10^7 s $^{-1}$) can be probed in dynamical deformation processes due to the limited time scales accessible to MD simulations [5,6]. These are to be contrasted with much slower experimental strain rates of 10^{-5} s $^{-1}$ to 10^{-3} s $^{-1}$ [7].

Over the past several years, a new extension to the phase field paradigm known as the *phase field crystal* (PFC) method [8–11] has emerged. This methodology can be viewed as a bridge between atomistic simulation and the traditional phase field approach. Similar to phase field technique, the system is described by a characteristic free-energy functional expressed in terms of a continuum field. In this case, however, the continuum field is a local time-averaged

number density $\rho(\vec{x}, t)$ endowed with the periodicity of a crystal lattice. Any disturbance or topological defect in the lattice will thus increase the free energy, capturing information which was until now inherent only to atomistic simulations. These include multiple crystal orientation, crystal defects, and elastic distortions of the lattice.

The original PFC model introduced by Elder and Grant is described by a free energy minimized by a hexagonal crystal lattice in two dimensions (2Ds) [9]. The dynamics of the model is diffusive, driven by a free-energy minimization and having a form of the Swift-Hohenberg equation. It was shown that the model naturally gives rise to polycrystalline grain boundaries, grain-boundary energies, and dislocations. A related model was also used to study melting in a presence of dislocations in three-dimensional bcc crystals [12]. The PFC model was also shown to accurately describe the dynamics of dislocation in climb and glide, the latter of which originally required the application of rigid transformations to emulate long-range elastic modes [13]. A modified PFC model (MPFC) introduced by us [10] made it possible to self-consistently simulate rapid elastic relaxation over long length scales through the introduction of higher-order time derivatives in the PFC dynamics. The MPFC model was later also derived from a treatment of solid hydrodynamics [14,15].

Recent work by Elder *et al.* [11] also linked the PFC methodology to the classical density-functional theory (DFT) of freezing [16] of materials with one or more components. This link was exploited to derive a new PFC model for binary alloys, the robustness of which was demonstrated in simulating phenomena such as dendritic growth, spinodal decomposition, and epitaxial growth. This work [11] also introduced a simple coarse graining procedure for deriving an alloy phase field model directly from the binary-alloy PFC model, demonstrating how the gradient energy terms in phase field models can be connected to microscopic theories.

Other treatments of the original PFC model [17] or more general DFT-based models [18,19] have shown that more sophisticated coarse graining procedures give rise to phase field-type models with complex order-parameter equations. Besides the connection of such complex order-parameter models to microscopic properties, they also provide a simple

way to model polycrystalline solidification and solid-state transformations. Moreover, working directly with amplitude representations of PFC or DFT models makes it possible to use adaptive mesh refinement [20] for significant increases in numerical efficiency.

The goals of this paper are twofold. First, it provides a thorough exposition of the MPFC model as well as a semi-implicit multigrid-based numerical scheme employed to efficiently solve the equations of motion. Second, we apply the MPFC model to elucidate deformation and plasticity in nanocrystalline (NC) materials with a relatively broad range of mean crystal sizes.

The rest of the paper is organized as follows. In Sec. II we introduce the MPFC approach, while the deformation behavior of nanocrystalline materials is presented in Sec. III. The paper concludes with a brief discussion in Sec. IV, while the details of the numerical algorithm can be found in the Appendix.

II. MODIFIED PHASE FIELD CRYSTAL MODEL

The MPFC formalism is based on minimization of the free-energy functional of atomic number density $\rho(\vec{r})$. In contrast to classical phase field approaches, which incorporate spatially uniform ground states, in the PFC approach the ground states are periodic (e.g., hexagonal in 2D and bcc in three dimension). Our starting point is a phenomenological free-energy functional

$$\mathcal{F} = \int d\vec{r} \left\{ \frac{\rho}{2} [r + c(k_0^2 + \nabla^2)^2] \rho + u \frac{\rho^4}{4} \right\}, \quad (1)$$

where $r \equiv a\Delta T$. The constant u is an adjustable parameter, set to $u=1$ in this work. The constants a and c are parameters that in general will depend on other parameters, such as density or pressure, and can be deduced from the shape of the correlation function for a specific material. It should be noted that the free energy in Eq. (1) can be derived from the two-point direct correlation function, as discussed in Ref. [11].

In its original phase field crystal model, the density field evolves according to

$$\frac{\partial \rho}{\partial t} = M \nabla^2 \mu = M \nabla^2 \frac{\delta F[\rho; T]}{\delta \rho}, \quad (2)$$

where M denotes a mobility and μ is the chemical potential. Physically, the above kinetic equation propagates all disturbances (elastic and plastic) diffusively. The motivation behind the development of a MPFC model is to include, besides diffusive dynamics, relaxation of elastic strains, which relax very rapidly compared to phenomena that evolve on diffusive time scales. The simplest way to achieve this is to make the MPFC dynamics operate on two time scales: one diffusional and the other corresponding to a propagating elastic mode. By choosing the effective sound speed α and the effective vacancy diffusion coefficient β , a finite elastic interaction length and time can be set. Over this elastic interaction time and distance, density waves will propagate effectively undamped. Beyond this time and distance, how-

ever, density evolution becomes diffusive. The simplest equation of motion that contains the above features is that of a damped (nonlinear) wave equation,

$$\frac{\partial^2 \rho}{\partial t^2} + \beta \frac{\partial \rho}{\partial t} = \alpha^2 \nabla^2 \frac{\delta F[\rho; T]}{\delta \rho}. \quad (3)$$

A rigorous treatment of solid hydrodynamics by Majaniemi and Grant [14] and Majaniemi and co-workers [15] showed that at late times and long length scales, Eq. (3) adequately describes phenomena evolving on diffusive time scales alongside those mediated by strain relaxation, which evolve on phonon times scales. It is noteworthy, however, that Eq. (3) is simulated on time scales many orders of magnitude longer than molecular dynamics, as will be discussed below.

A simple phenomenological derivation that motivates the derivation to Eq. (3) can be developed as follows. Treating the system as a continuum and combining the continuity equation $\partial \rho / \partial t = -\nabla \cdot \vec{g}$ with the divergence of the momentum conservation equation $\partial g_i / \partial t = -\partial (g_i g_j / \rho) / \partial x_j - \partial p / \partial x_i$, where the pressure is given by $p = -f + \rho \delta F / \delta \rho$ yields $\partial^2 \rho / \partial t^2 = \nabla_i (\rho \nabla_i \mu) + \mathcal{O}(g^2)$ (where repeated indices are summed over). By construction, this equation conserves mass, and its linearized form (around $\rho = \rho_0$) supports propagating density wave solutions with an effective sound speed $c = \sqrt{\rho_0 (\partial \mu / \partial \rho)}|_{\rho = \rho_0}$. We generalize this to a spatially periodic ρ , employ the approximation $\nabla_i (\rho \nabla_i \mu) \approx \alpha^2 \nabla^2 \mu$, and incorporate dissipation by adding a term $\beta \partial \rho / \partial t$.

Linear stability analysis

To better understand the dynamics governed by the MPFC equation, we perform a Floquet analysis, which linearizes Eq. (3) around the equilibrium density field ρ_{eq} according to

$$\rho_p = \rho_{eq} + \delta \rho, \quad (4)$$

where

$$\begin{aligned} \rho_{eq} &= \rho_0 + \sum_{n,m} a_{n,m} e^{i\vec{G}_{n,m} \cdot \vec{r}}, \\ \delta \rho &= \sum_{n,m} b_{n,m}(t) e^{i\vec{G}_{n,m} \cdot \vec{r} + i\vec{Q} \cdot \vec{r}}, \end{aligned} \quad (5)$$

with ρ_0 as the average density, $\vec{G}_{n,m} = n\hat{x} + (n+2m)/\sqrt{3}\hat{y}$ as the triangular reciprocal-lattice vectors, and $a_{n,m}$ as their corresponding amplitudes. The vector \vec{Q} is a perturbation wave vector and $b_{n,m}(t)$ is the corresponding amplitude associated with the perturbation of the steady-state mode (m, n) . The linear form of Eq. (3) is obtained by substituting Eq. (4) into Eq. (3) and expanding the latter to linear order in $\delta \rho$. The resulting linearized equation of motion of the fastest growing mode $m=n=0$ is given by

$$\frac{d^2 b_{0,0}}{dt^2} + \beta \frac{db_{0,0}}{dt} = -\alpha^2 Q^2 \left\{ 3\rho_0^2 + r + (q_0^2 - Q^2)^2 + \frac{9}{8} A_{\min} \right\} b_{0,0}. \quad (6)$$

Equation (6) describes how density perturbations grow, decay, or propagate. Specifically, the leading-order mode satisfies $b_{0,0} \sim e^{i\omega t}$ with the dispersion relation

$$\omega(Q) = i\frac{\beta}{2} \pm \frac{\Lambda(Q)}{2}, \quad (7)$$

where

$$\Lambda(Q) = \sqrt{-\beta^2 + 4\alpha^2 Q^2 \left[3\rho_o^2 + r + (Q^2 - q_o^2)^2 + \frac{9}{8}A_{\min}^2 \right]}. \quad (8)$$

The parameter

$$A_{\min} = \frac{4}{5} \left(\rho_o + \frac{1}{3} \sqrt{-15r - 36\rho_o^2} \right) \quad (9)$$

denotes the amplitude of ρ_{eq} within a single-mode approximation, as originally derived in Ref. [9].

Within the window of wave vectors delineated by $Q^2 \ll q_o^2$ and

$$4\alpha^2 Q^2 [3\rho_o^2 + r + \lambda(Q^2 - q_o^2)^2 + 9/8A_{\min}^2] \gg \beta^2, \quad (10)$$

the dispersion relation reduces to

$$\omega(Q) \equiv i\frac{\beta}{2} \pm v_{eff}Q = i\frac{\beta}{2} \pm 2\alpha Q \sqrt{3\rho_o^2 + r + q_o^4 + \frac{9}{8}A_{\min}^2}. \quad (11)$$

The dispersion Eq. (11) describes a pair of density waves that propagate essentially undamped for time $t_w \approx 2\beta^{-1}$ over a length scale

$$\bar{L} \sim v_{eff}t_w = 4\alpha \sqrt{3\rho_o^2 + r + q_o^4 + 9/8A_{\min}^2} / \beta. \quad (12)$$

Conversely, on length scales beyond \bar{L} or on time scales greater than t_w , density evolution becomes diffusive. Specifically, in the limit $\bar{Q} \rightarrow 0$, the dispersion relation reduces to two pure imaginary modes $\omega_1 = i\beta$ and $\omega_2 = iQ^2\alpha^2(3\rho_o^2 + r + q_o^4 + \frac{9}{8}A_{\min}^2)/\beta$ with $|\omega_1| \gg |\omega_2|$. Asymptotically, $b_{0,0}(t) \sim \exp(-|\omega_2|t) \equiv \exp(-DQ^2t)$, where D denotes the effective vacancy diffusion coefficient; thus

$$D = \frac{\alpha^2}{\beta} \left(3\rho_o^2 + r + q_o^4 + \frac{9}{8}A_{\min}^2 \right). \quad (13)$$

The above analysis demonstrates that Eq. (3) admits propagating solutions for density disturbances with an effective elastic interaction length \bar{L} and interaction time $t_{eff} = t_w$, which can be tuned to the specific system parameters. As an illustration, let $L^* = \max[L_x, L_y]$ denote the largest dimension of the system under consideration and define $\Delta \equiv (3\rho_o^2 + r + q_o^4 + 9/8A_{\min}^2)$. Since $D = \alpha^2\Delta/\beta$, $\bar{L} \approx 4\alpha\sqrt{\Delta}/\beta$, and we require, for the entire system to relax strain “instantaneously,” that

$$\bar{L} = \frac{4D}{\alpha\sqrt{\Delta}} \geq L^* \quad (14)$$

or

$$\alpha \leq \frac{4D}{L^*\sqrt{\Delta}}. \quad (15)$$

After choosing a value of α that satisfies Eq. (15), β is determined from

$$\beta = \frac{\alpha^2\Delta}{D}. \quad (16)$$

For example, to simulate a system with a vacancy diffusion coefficient $D \approx 10^{-18}$ m²/s and a currently feasible system size $\bar{L} \approx 1$ μ m, one would choose $\alpha = 4 \times 10^{-12}$ m/s for the effective speed of sound and the damping coefficient $\beta = 1.6 \times 10^{-5}$ s⁻¹. This sound speed is to be contrasted with classical MD simulations, where $\alpha \sim 10^3$ m/s by necessity; that is, $\alpha_{MD}/\alpha_{MPFC} \sim 10^{15}$.

In short, the MPFC approach takes advantage of the fact that elastic relaxation does not need to be instantaneous as long as separation of time scales exists between diffusive and elastic phenomena—such relaxation is *effectively* instantaneous. This approach is employed below to elucidate deformation behavior of nanocrystalline metals.

III. MPFC STUDY OF DEFORMATION MECHANISMS IN NANOCRYSTALLINE METALS

The successful application of nanocrystalline metals as structural materials in industrial applications requires a detailed knowledge of mechanical properties and understanding of deformation behavior. Hall [21] and Petch [22] studied materials on a microcrystalline level and found linear relationship between the yield strength σ_y and the inverse square root of the grain diameter d . This theory was rationalized through the *pileup* of dislocations at grain boundaries created in the process of plastic deformation. An important question is what happens as the grain size decreases to less than ≈ 100 nm.

For average grain sizes in the range of 100–200 nm (also called an ultrafine grain size), the yield strength can increase to approximately 400 MPa for most pure materials, more than double that of their microcrystalline counterparts [23–25]. More detailed exploration of ultra fine crystalline (UFC) silver samples by high resolution electron microscopy (HREM) confirmed signs of plasticity in grains with sizes of 200 nm [26]. Deformation strains concentrated inside the grains suggested that dislocation-mediated deformation is the dominant deformation mechanism in ultrafine grained materials.

Because of the small size of most NC samples, studies of strength are usually confined to hardness measurements. Chokshi *et al.* were the first to report a decrease in hardness with a decrease as grain size decreased from 20 to 5 nm for NC copper and palladium produced by IGC [27]. This has been coined the reverse Hall-Petch effect (HPR). Deviations from the HPR were also observed in studies on NC samples of Ni-P alloy with average grain sizes less than 37 nm [28], NC nickel with average grain sizes less than 20 nm [29], and Al-1.5%Mg alloy [30]. More recent measurements on copper found grain-size strengthening down to 10 nm [31], while

achieving compressive strength up to 3 GPa. Besides the high strength, this study demonstrates that variation in production methods can have a strong influence on nanocrystalline materials properties.

It was suggested in the early days of NC materials that below the critical grain size—in other words, below the size when dislocation activity has ceased—the mechanism for deformation will be creeplike based on *Coble creep* [27,32]. Even though the calculation for copper suggested creep rates of $6 \times 10^{-3} \text{ s}^{-1}$ for $\sigma=100 \text{ MPa}$ and $d=5 \text{ nm}$, direct creep measurements on NC Cu a Pd did not support this explanation [33], suggesting a different explanation for the reverse Hall-Petch effect.

On the other hand, some MD simulations [5] of defect free NC samples did suggest creeplike deformation mechanism with strain rates consistent with Coble creep mechanism. Other MD simulations [6,34] and theoretical studies [35] also suggested a deformation by the grain-boundary sliding mechanism. However, it was pointed out that these two processes must act in parallel to prevent internal void or cracks. After the grain is deformed by diffusional creep, one dimension is extended and the other lowered; to compensate for this change grain boundaries must slide by exactly the distance changed by diffusional creep [36].

The remainder of this section reports MPFC simulations of polycrystalline samples with different grain sizes under uniaxial tensile load, done in order to explore nanocrystalline deformation mechanisms and strength. We begin by discussing the initial conditions, boundary conditions, and the setup of our simulations.

A. Initial conditions and boundary conditions

For all samples, periodic boundary conditions in all directions were used. Polycrystalline solid samples with the hexagonal crystal structure were placed in the pool of liquid that surrounded them on all four sides. This was achieved by choosing values of r and ρ_0 from the coexistence region of the hexagonal solid and liquid phase diagram [9]. Using a lever rule, the amounts of liquid and solid in the simulated sample were set with no preference toward crystallization or melting.

To prepare polycrystalline samples containing grains with various orientations, seeds with hexagonal symmetry and random orientations were seeded into an undercooled liquid. Initial seeds were grown at a “temperature” parameter of $r=-0.3$ in the phase diagram, in order to prevent the formation of faceted grain boundaries. Samples grown to a specific size were then placed into a surrounding pool of liquid at a lower temperature ($r=-0.6$). The ratio of the liquid to solid was consistent with the lever rule at coexistence at $r=-0.6$. As a result, we obtained polycrystalline samples surrounded by liquid from all sides. The number of initial seeds defined the final number of grains and, thus, the average grain size. After the simulation setup, all samples were left to equilibrate until the free energy did not change with time.

B. Strain application

Samples were deformed by uniaxial tensile load, applied through traction boundary conditions. Traction boundary

conditions were incorporated into the phase field crystal model using a new penalty term [10] implemented into the MPFC model. The penalty term is a positive-definite term in the free energy of Eq. (1). It is the square of the difference of the density field and the imposed density field ρ_s comprising an external surface. To emulate the boundary traction—or the traction at specific locations in the sample—the penalty term is modulated by a function $M(\vec{x})$, that is, equal to zero outside the zone where the traction is being applied. By adding a penalty term in the form of $M(\vec{x})(\rho-\rho_s)^2$, the free energy becomes

$$\mathcal{F} = \int d\vec{r} \left\{ \frac{\rho}{2} [a\Delta T + c(k_0^2 + \nabla^2)^2] \rho + u \frac{\rho^4}{4} + M(\vec{x})(\rho - \rho_s)^2 \right\}. \quad (17)$$

A convenient feature of this approach is that the modified free energy in Eq. (17) has exactly the same phase diagram as that in Eq. (1).

To study single-crystal deformations, the shape of the density field of the traction surface ρ_s is in the form of a single-mode approximation of the hexagonal crystal structure. To accommodate various crystal orientations, on the other hand, the traction surface density function was written as a series of Gaussians in two dimensions, refitted to the periodic density field of the sample over the range of interest. That is,

$$\rho_s(x, y) = A \sum_{i=1}^N e^{-\sigma[(x-x_i)^2 + (y-y_i)^2]}, \quad (18)$$

where A is an amplitude, $\{x_i, y_i\}$ ($i=1, \dots, N$) denote the N locations of peaks in ρ_s and σ sets the width of density peak around each atom (chosen to be equal to one half of the equilibrium lattice spacing of the hexagonal lattice).

C. Strain measurements and data interpretation

Strain in the sample and the positions of the dislocations were identified by locating peaks in the density field $\rho(x, y)$; these peaks were identified with atoms in the corresponding crystalline aggregate. The average strain was calculated by comparing the distance to an atom’s nearest neighbors with the corresponding distance in a perfect crystal (i.e., the lattice parameter a_x). If the distance to any nearest neighbor increased by da_x , the local strain was then calculated as da_x/a_x . The calculation was repeated over all six neighbors of an atom and the average local strain was taken as $d\bar{a}_x = (da_{x1} + da_{x2} + \dots + da_{x6})/6$. This calculation was repeated over all N atoms in the sample, yielding an average strain

$$\bar{\epsilon} = \frac{1}{6Na_x} \sum_{i=1}^N d\bar{a}_{xi}. \quad (19)$$

D. Characterization of samples

Samples were grown by heterogeneous nucleation, which generated multiple grain orientations. To facilitate the analysis of simulations, we identified what atoms were located at

TABLE I. Samples overview.

Sample number	Sample size [grid size]	Number of grains []	Average grain-size Cu example (nm)
1	1025 × 1025	6	14.88
2	1025 × 1025	15	7.94
3	1025 × 1025	18	7.78
4	1025 × 1025	19	7.67
5	1025 × 1025	30	6.45
6	1025 × 1025	23	6.84
7	1025 × 1025	40	4.97
8	2049 × 2049	10	29.25
9	2049 × 2049	18	21.57
10	2049 × 2049	20	20.42
11	2049 × 2049	37	14.69
12	2049 × 2049	37	14.73
13	2049 × 2049	53	12.06
14	2049 × 2049	54	12.04
15	2049 × 2049	86	9.4
16	4098 × 4098	9	48.1

the grain boundaries, around dislocations, or inside the grain by determining the local crystalline order around an atom. Atoms in perfect hexagonal order—or those having six-nearest neighbors—are considered to be inside a perfect crystal, while those with less than six-nearest neighbors are considered to be at a free surface, grain boundary, or within a dislocation core.

We studied nanocrystalline samples in one of three numerical grids: the first ($1025\Delta x \times 1025\Delta x$) was used for samples with smaller average grain sizes, the others $2049\Delta x \times 2049\Delta x$ and $4097\Delta x \times 4097\Delta x$ were used for samples containing larger grain sizes. For these system sizes, samples contained approximately 2×10^4 , 8×10^4 , and 3.2×10^5 atoms, respectively. Using copper as an example, with a lattice parameter of 3.6 Å, these sample sizes correspond approximately to $50 \times 50 \text{ nm}^2$, $100 \times 100 \text{ nm}^2$, and $200 \times 200 \text{ nm}^2$, respectively. In total, 16 samples with grain sizes ranging from 5 to 50 nm were prepared. The properties of the individual samples are listed in Table I.

E. Numerical implementation

Boundary loads were applied to 30 atomic rows of a square sample (which was surrounded by liquid) from two sides. After equilibration of the samples, a uniaxial tensile load was applied at a slow constant strain rate of $0.001/\Delta t$ by displacing the penalty function. During the simulation, the free energy was calculated using Eq. (1) from the density profiles of $\rho(x, y)$. The average strain in the sample was calculated at every 2000 time steps. For this study, the model parameters $\alpha=200$, $\beta=0.5$ were used. In order to simulate the model efficiently with these parameters, a semi-implicit multigrid solver was developed for the MPFC equation. The details of this numerical algorithm and its convergence and efficiency properties are detailed in the Appendix.

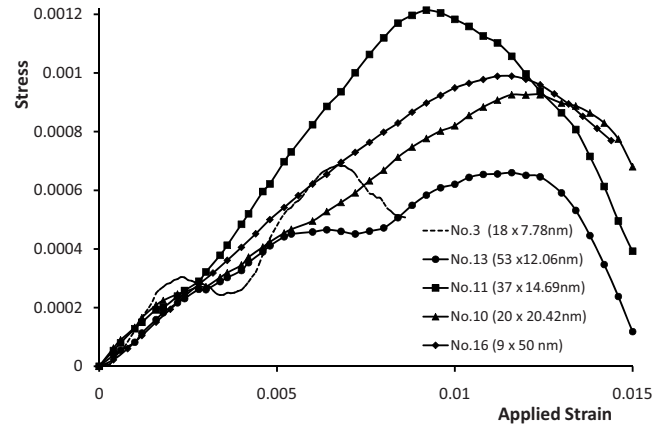


FIG. 1. Stress-strain curves for five simulations with varying grain size. To analyze the strength, the stress in the sample was calculated as $\sigma = dF/d\epsilon_{yy}$, where ϵ_{yy} is the applied uniaxial strain.

F. Simulation results

Samples with grain size above ≈ 15 nm initially deformed elastically (Fig. 1). At about 1% of deformation, individual dislocation gliding events occurred in order to relieve stress. A typical example of this behavior is seen by following dislocations A and C in Fig. 2. The dislocations either relaxed toward the sample surface, creating a ledge (dislocation A, Fig. 2) or were absorbed by a grain boundary (dislocation C, Fig. 2). When all individual dislocations were exhausted upon further loading, the load was carried only by the grain boundaries. Even the largest grains (≈ 50 nm) were too small for traditional sources (such as the Frank-Read source) to operate. Grain boundaries remained the only possible source of dislocations in two dimensions.

We observed low-angle grain boundaries that decayed and acted as a dislocation source (dislocation B, Fig. 2), thus, contributing gliding dislocations to the plastic flow. As the dislocation left the low-angle grain boundary, the original grain rotated and was extended into a neighboring grain, effectively causing a grain growth. These observations are consistent with high-resolution TEM (HRTEM) studies on nanocrystalline Ag by Ichikawa *et al.* [26]. In Fig. 3, a portion of the sample within a small grain is displayed. At about 1% deformation, the grain boundary of the parent grain started to decay through dislocation glide. As a result, the grain rotated about 2° and its diameter decreased. This is consistent with findings of Murayama *et al.* [37], who observed rotational movement of grain in HRTEM of Fe.

As the grain size decreased below ≈ 15 nm, the fraction of the grain boundaries in the sample increased and fewer individual dislocations were observed. Moreover, some individual dislocations were “trapped” in the center of small grains and were prohibited from gliding. Upon loading, most of the stress was immediately transferred to the grain boundaries. Initially, the deformation was accommodated by a series of short gliding events of free dislocations. Similarly to the behavior in larger grains, low-angle grain boundaries decayed and became sources of mobile dislocations. Contrary to the first case, however, fracture, void creation, and growth were observed at triple junctions, crystal surfaces, and high-

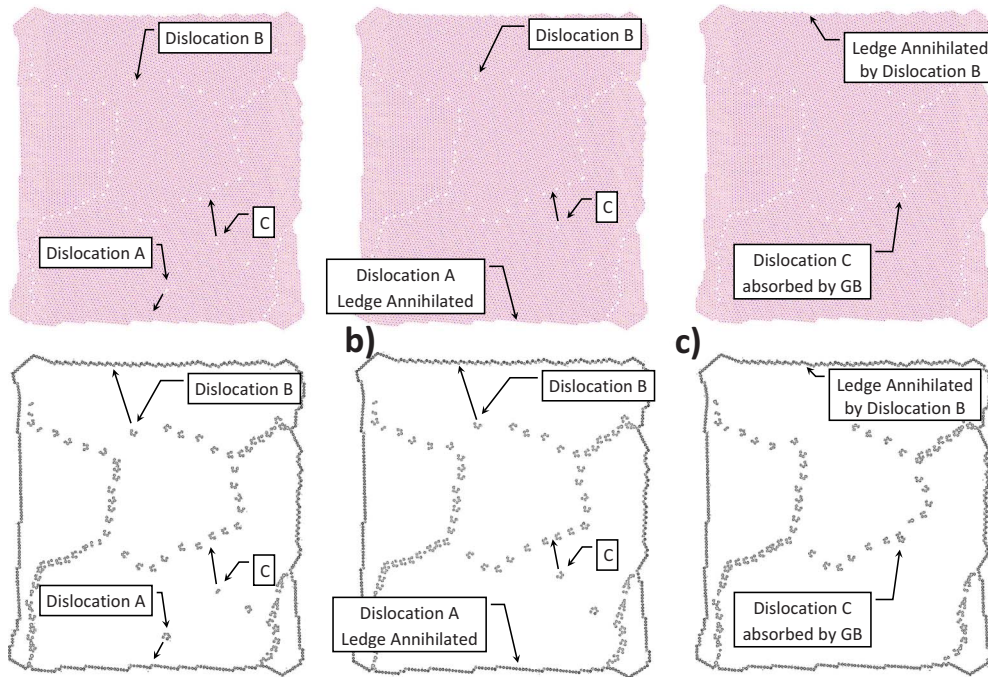


FIG. 2. (Color online) Three time slides capturing deformation in the $50 \times 50 \text{ nm}^2$ sample. Average grain size is 15 nm. Dislocations A and C are absorbed by the surface or grain boundary, respectively. Dislocation B is ejected from the grain boundary (GB) and annihilated at the surface. Small arrows without labels point to a dislocation trajectory.

angle grain boundaries. Once a nanovoid was nucleated, the resulting stress-free surface of the void caused localized stress and strain concentrations. Free dislocations and dislocations generated from the grain boundaries glided toward the strain concentrations to relieve the stress. The process can be described as periodic nanovoid growth and nanovoid healing through the annihilating of dislocations. This behavior manifested itself as a plateau on stress-strain curves of samples with smaller grain sizes (samples 3 and 13 in Fig. 1). Once there was no mobile dislocation available in the proximity to the void, the deformation continued through the void growth and fracture, as depicted in Fig. 4. The formation of cracks at triple junctions and grain boundaries for lower grain sizes was reported in experimental works by Kumar *et al.* [38].

The yield point was determined to be the intersection between the stress-strain curve (Fig. 1) and a line parallel to the

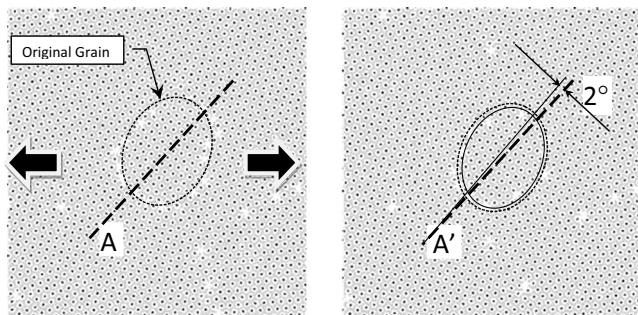


FIG. 3. Two frames showing a portion of a sample with a rotating grain. Initial time is $t=30$ and final time is $t=40$. Dashed lines A and A' are parallel. The dotted line shows the original shape of the grain. It is superimposed onto the deformed grain on the right.

linear part of the curve at 0.002 of the applied strain. When yield stress in the samples was plotted against the grain size, we found an increase in the yield stress with increasing grain size that suggested a “reversed” Hall-Petch effect on a nano-scale, as seen in Fig. 5. Figure 5 compares the MPFC simulations results (solid points) with experimental results (empty points) [39]. The data are rescaled with respect to the “strongest size,” i.e., grains size with the highest strength. The

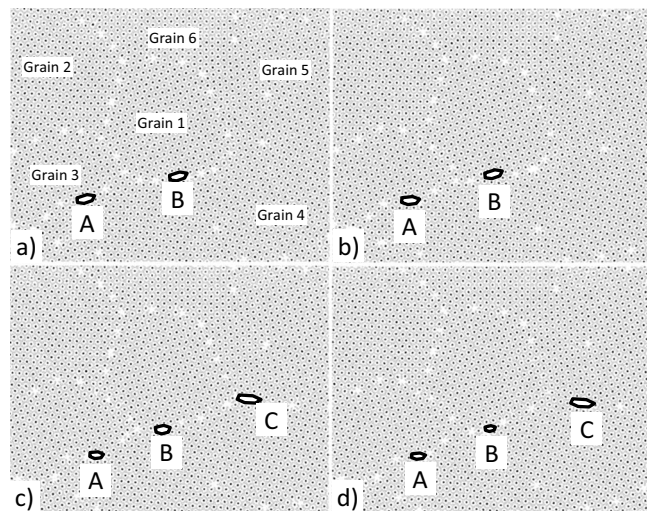


FIG. 4. Three voids A, B, and C are displayed in four consecutive times 25, 35, 45, and 50. Voids A and B are nucleated and continue to grow as simulation proceeds. In the second half [slides (c) and (d)], a third void C is nucleated, while the A and B voids are almost annihilated. It is interesting to point out the dynamic nature of the process evidenced by the voids “gliding” along grain boundaries.

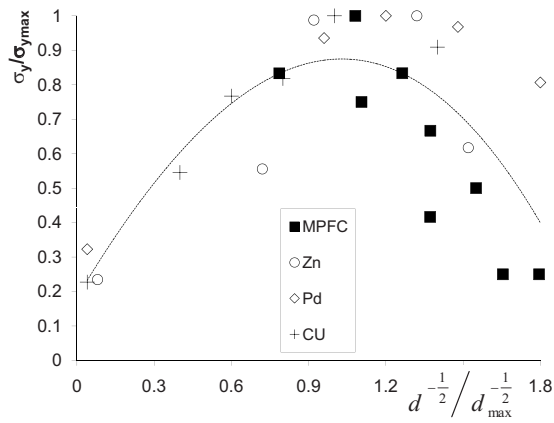


FIG. 5. Hall-Petch-type plot with yield stress plotted against the inverse square root of grain size. Solid points represent MPFC simulation results. Unfilled circles and diamonds are experimental measurements [39]. The data are rescaled about the highest stress and the corresponding grain size. The dashed line is a guide for the eyes.

MPFC model self-consistently is seen to capture the reverse Hall-Petch effect, in agreement with experimental data. At scales above 15 to 20 nm, our simulation data are also consistent with a plateau occurring in the experimental data at about 50 nm grain size—a shift to regular strengthening behavior. Thus, our simulations reveal that an increasing ratio of grain boundaries to bulk material in NC materials leads to a shift from dislocation-mediated deformation to deformation carried by grain boundaries followed by void creation.

IV. DISCUSSION AND CONCLUSIONS

In this paper, we presented details and applied two extensions to the *phase field crystal* modeling technique. We coined our model, a MPFC model. This methodology offers a unique combination of accessible length scales and time scales, which is suitable to address the deformation and NC materials phase transformation problems. The MPFC method exploits separation of time scales by introducing instantaneous to the diffusional time scale of the original PFC model. Separation of the time scales is controlled by the tunable parameters α and β , which are related to the effective speed of sound and the vacancy diffusion coefficient, respectively. Stability analysis of the linearized equation of motion showed a critical elastic length scale that sets the distance over which the disturbance will travel instantaneously.

In an examination of grain-size dependence on the yield strains, we found a decreasing trend with decreasing grain size, which suggests a reversed Hall-Petch behavior. We also observed a plateau in the yield strain plot for grain sizes above 15 nm. At about 15 nm in grain size, the deformation regime changed from a dislocation-controlled regime to one where most of the deformation was carried by grain boundaries and manifested itself in grain rotation, grain growth, void nucleation and growth.

We developed an efficient solver using a multigrid technique for numerical solution of the MPFC model. We measured its computational efficiency and convergence and found an improvement in both measures compared to traditional iterative solvers. Moreover, we found increased stability as compared with explicit time—marching scheme used previously.

It is expected that both the alloy MPFC formalism will play an important role in self-consistently linking material properties to microstructure development in a manner that *fundamentally* links the mesoscale to the atomic scale.

ACKNOWLEDGMENTS

This work has been in part supported by the National Science and Engineering Research Council of Canada (N.P.) and an NSF-DMR Grant No. 0449184 (M.H.).

APPENDIX: SEMI-IMPLICIT SOLVER DEVELOPMENT FOR EFFICIENT SIMULATION

To simulate the MPFC model efficiently, we developed an implicit algorithm to overcome the limitations imposed by explicit methods, particularly, at higher wave speeds. There were two reasons for choosing the multigrid approach. The first, which will be demonstrated in this section, is that it is the only iterative method competitive with Fourier methods. The second is that since multigrid is a real-space algorithm, it is a trivial matter—unlike Fourier methods—to impose almost any type boundary conditions. This makes very simple, for example, to specify tractions or strains at boundaries, a feature critical to the study of elastoplastic effects, for which the MPFC model was developed.

1. Discretization of MPFC model

The main challenge in simulating the MPFC equation is posed by the sixth-order space derivative, which introduces time step restrictions stiffness. The stability of an explicit method requires approximately that $\Delta t \leq \beta(\Delta x^6/2\pi)/\alpha^2$. For this study $\alpha=200$, $\beta=0.5$, and $\Delta x=\pi/4$, $\Delta t \leq 10^{-8}$, which becomes prohibitively small. Another challenge is that there is a cubic nonlinear term on the right-hand side that further contributes to overall stiffness of the equation. To avoid the sixth-order derivative limitation, we split the equation into a system of three second-order equations as follows:

$$\frac{\partial^2 \rho(\mathbf{x})}{\partial t^2} + \beta \frac{\partial \rho(\mathbf{x})}{\partial t} = \alpha^2 \nabla^2 \mu(\mathbf{x}),$$

$$\mu(\mathbf{x}) = r\rho(\mathbf{x}) + \rho(\mathbf{x}) + 2v + \nabla^2 v(\mathbf{x}) + \rho(\mathbf{x})^3,$$

$$v(\mathbf{x}) = \nabla^2 \rho(\mathbf{x}), \quad (\text{A1})$$

where $\mathbf{x}=(x_1, x_2) \in \Omega$ and $\Omega \subset R$ is a given domain.

We discretize the system of Eqs. (A1) in 2D space as

$$\frac{\partial^2 \rho_h(x, y)}{\partial t^2} + \beta \frac{\partial \rho_h(x, y)}{\partial t} = \alpha^2 \nabla^2 \mu_h(x, y),$$

$$\mu_h(x, y) = r \rho_h(x, y) + \rho_h(x, y) + 2v_h + \nabla^2 v_h(x, y) + \rho_h(x, y)^3,$$

$$v_h(x, y) = \nabla^2 \rho_h(x, y),$$

$$[(x, y) \in \Omega_h], \quad (\text{A2})$$

where h is a discretization parameter characterizing a square uniform grid and $\Omega_h = \{(x, y) : x = x_i = ih, y = y_j = jh; 1 \leq i \leq N, 1 \leq j \leq N\}$. For increased stability in the solution of Eq. (3) as well as the ability to use a larger time step than explicit methods, we discretize the system of Eqs. (A2) using an implicit algorithm in time,

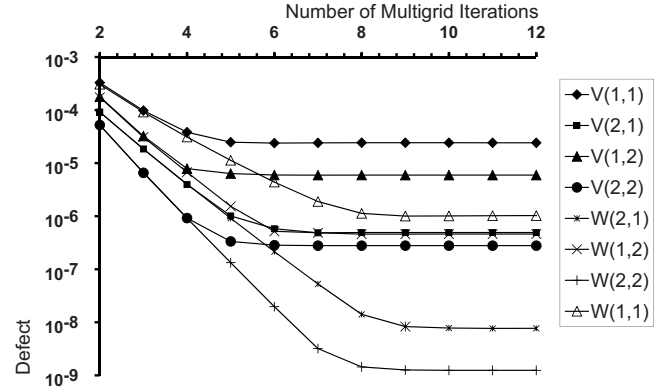


FIG. 6. The convergence history of different multigrid cycles for a typical run of the MPFC model during a solidification experiment.

$$\begin{aligned} \frac{\rho_{i,j}^{n+1} - 2\rho_{i,j}^n + \rho_{i,j}^{n-1}}{dt^2} + \beta \frac{\rho_{i,j}^{n+1} - \rho_{i,j}^{n-1}}{2dt} &= \alpha^2 \frac{\mu_{i-1,j}^{n+1/2} + \mu_{i+1,j}^{n+1/2} + \mu_{i,j+1}^{n+1/2} + \mu_{i,j-1}^{n+1/2} - 4\mu_{i,j}^{n+1/2}}{h^2}, \\ \mu_{i,j}^{n+1/2} &= \rho_{i,j}^{n+1} + r\rho_{i,j}^{n+1} + 2v_{i,j}^{n+1} + \frac{v_{i-1,j}^{n+1} + v_{i+1,j}^{n+1} + v_{i,j+1}^{n+1} + v_{i,j-1}^{n+1} - 4v_{i,j}^{n+1}}{h^2} + \hat{\phi}(\mu_{i,j}^n, \mu_{i,j}^{n+1}), \\ v_{i,j}^{n+1} &= \frac{\rho_{i-1,j}^{n+1} + \rho_{i+1,j}^{n+1} + \rho_{i,j+1}^{n+1} + \rho_{i,j-1}^{n+1} - 4\rho_{i,j}^{n+1} + \rho_{i-1,j}^n + \rho_{i+1,j}^n + \rho_{i,j+1}^n + \rho_{i,j-1}^n - 4\rho_{i,j}^n}{2h^2}, \end{aligned} \quad (\text{A3})$$

where $\hat{\phi}(\mu_{i,j}^n, \mu_{i,j}^{n+1}) = (\rho_{i,j}^{n+1})^3$ is linearized nonlinear part.

2. Iterative multigrid solver

The system of Eqs. (A3) can, in principle, be solved iteratively by a method such as Gauss-Seidel method or successive over-relaxation (SOR) [40]. In order to do that, the nonlinear part can be linearized as follows:

$$\hat{\phi}(u_{i,j}^n, u_{i,j}^{n+1}) = \hat{\phi}(u_{i,j}^n, u_{i,j}^m) + \frac{\partial \hat{\phi}(u_{i,j}^n, u_{i,j}^m)}{\partial u} (u_{i,j}^{n+1} - u_{i,j}^m), \quad (\text{A4})$$

$$\begin{aligned} \hat{\phi}(u_{i,j}^n, u_{i,j}^{n+1}) &= \hat{\phi}(u_{i,j}^n, u_{i,j}^m) + \frac{\partial \hat{\phi}(u_{i,j}^n, u_{i,j}^m)}{\partial u} (u_{i,j}^{n+1} - u_{i,j}^m) \\ &= \frac{1}{2}(u_{i,j}^{n3} + u_{i,j}^{m3}) + \frac{3}{2}(u_{i,j}^{n2} + u_{i,j}^{m2})(u_{i,j}^{n+1} - u_{i,j}^m). \end{aligned} \quad (\text{A5})$$

Then Eq. (A5) is substituted into the second equation of Eqs. (A3), and $u_{i,j}^{n+1}$ terms are replaced by $u_{i,j}^{m+1}$ iteration terms. The system of Eqs. (A3) is then solved iteratively while for each iterative step a following 3×3 matrix is inverted.

Rearranging Eqs. (A3), the iteration formulas read as

$$\begin{aligned} &\begin{pmatrix} \beta dt/2 + 1 & 4\alpha^2 dt^2/h^2 & 0 \\ (-1-r) - 3/2(\rho_{i,j}^{n2} + \rho_{i,j}^{m2}) & 1 & 4/h^2 - 2 \\ 2/h^2 & 0 & 1 \end{pmatrix} \begin{pmatrix} \rho_{i,j}^{m+1} \\ \mu_{i,j}^{m+1/2} \\ v_{i,j}^{m+1} \end{pmatrix} \\ &= \begin{pmatrix} 2\rho_{i,j}^n + \rho_{i,j}^{n-1}(\beta dt/2 - 1) + 4\alpha^2 dt^2/h^2(\mu_{i-1,j}^{m+1/2} + \mu_{i+1,j}^{m+1/2} + \mu_{i,j+1}^{m+1/2} + \mu_{i,j-1}^{m+1/2}) \\ (v_{i-1,j}^{m+1} + v_{i+1,j}^{m+1} + v_{i,j+1}^{m+1} + v_{i,j-1}^{m+1})/h^2 + 1/2(\rho_{i,j}^{n3} + \rho_{i,j}^{m3}) - 3/2(\rho_{i,j}^{n2} + \rho_{i,j}^{m2})\rho_{i,j}^n \\ (\rho_{i-1,j}^{m+1} + \rho_{i+1,j}^{m+1} + \rho_{i,j+1}^{m+1} + \rho_{i,j-1}^{m+1} + \rho_{i-1,j}^n + \rho_{i+1,j}^n + \rho_{i,j+1}^n + \rho_{i,j-1}^n - 4\rho_{i,j}^n)/2h^2 \end{pmatrix}, \end{aligned} \quad (\text{A6})$$

TABLE II. Wall-clock times and corresponding number of iterations for a defect reduction by a factor 10^{-6} for different cycles when solving Eq. (3) under conditions similar to those of Fig. 6.

Multigrid cycle	Iteration steps	Time (sec)
V(2,1)	5	2.45
V(2,2)	4	2.47
W(2,1)	5	7.02
W(2,2)	4	7.11

where the m and $m+1$ terms are approximations before and after iteration, respectively, and we have redefined $h \rightarrow \Delta x$. For each iteration step, we solve Eq. (A6) by solving a 3×3 matrix at each node. A severe problem with traditional solvers is that they require of N^2 order iterations to converge to the answer of the next time step, where N is the number of nodes on a numerical mesh (see also Fig. 7). To circumvent this problem, we applied the *multigrid method* to the solution of the MPFC equation of motion, using a so-called full approximation scheme [41,42].

In the practice of multigrid, Eq. (A6) is solved to convergence only the coarsest level, while this is only iterated several times (per physical time step) on all finer levels. For this reason, multigrid is generally the fastest iterative algorithm. Except for the finest level of refinement, the source term on the right-hand side of Eq. (A6) is replaced by errors terms—or *defects*—carried over from the iteration on a finer level of the mesh. One sweep of iterations from finest level of refinement to coarsest level and back to the finest is referred to as a “V cycle.” Another possibility is a *W cycle*, wherein a V cycle returns to an intermediate level of refinement, before returning to the coarsest level and back again to the finest level of refinement.

By measuring the value of the defect (usually in terms of L_2 norm) between multigrid iteration cycles, we can determine if the defect is reduced (i.e., whether the multigrid method converges or not). Convergence depends on the type of cycle, V or W, defined by a cycle index $\gamma=1,2$, respectively, and the number of presmoothing and postsmoothing steps ν_1 and ν_2 , respectively, performed on the finest level of refinement. An example of the notation used to express a multigrid V cycle is $V(0,1)$, i.e., $\gamma=1$, with no presmoothing steps and one postsmoothing step. Another example $W(2,1)$ is a W cycle, i.e., $\gamma=2$, with $\nu_1=2$ and $\nu_2=1$. Figure 6 plots the defect as a function of multigrid cycles for a number of combinations of V and W cycles. The figure suggests rapid convergence of the multigrid for cycles $V(2,1)$, $V(2,2)$, $W(2,1)$, and $W(2,2)$. They can reduce the defect by a factor of 10^{-6} to 10^{-9} within six multigrid iterations. Also, the benefits of processing the coarse grid levels more frequently are evidenced by much better convergence of W cycles.

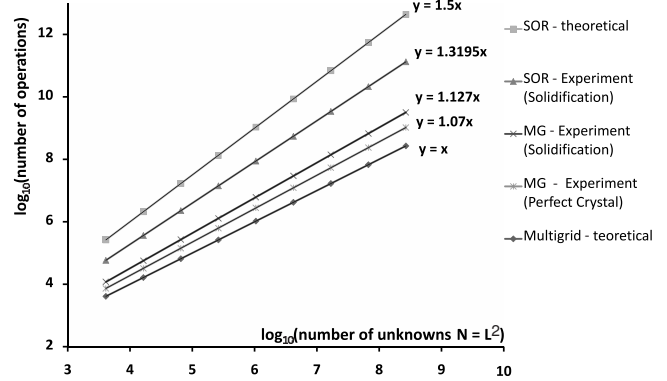


FIG. 7. Iterations to convergence vs number of grid points for successive over-relaxation (SOR) and multigrid (MG) methods. Both methods are solving model (3). The top and bottom lines represent the theoretical complexity for the SOR and multigrid approaches, respectively. The SOR and multigrid are further compared during a solidification simulation, where the iterative method increases the number of operations by a factor of 1.3 with increasing sample size, while multigrid method increases the same by a factor of 1.1. The performance of the multigrid approach improved very slightly when simulating a deformation in a perfect crystal. In this case, the number of operations increased 1.07 times with the number of computational nodes.

In order to choose the most efficient solver, it is necessary to look at both its convergence rate in terms of iteration cycles but also the overhead cost of a given type of cycle. In practice, the “real time” needed to achieve the solution is the most interesting value. Table II shows wall-clock times and number of iterations for a defect reduction by a factor 10^{-6} for different cycles. The times were measured during above convergence measurements and were done on the same computer work station. The table gives a different perspective from Fig. 6. Specifically, while both W cycles [$W(2,1)$ and $W(2,2)$] converge in the least number of iterations, their wall-clock time measurements are the slowest, with calculation times almost three times larger than the V cycles [$V(2,1)$ and $V(2,2)$]. For these reasons, we chose the $V(2,1)$ multigrid cycle as our primary method for the large deformation simulations described in the following section.

As a consistency check, we also compared the convergence efficiency of our multigrid algorithm against that for successive over-relaxation. Figure 7 plots the number of iterations to convergence vs the number of grid points in a mesh. The straight lines are fits for each solution method. For two different initial conditions, our multigrid algorithm closely follows the theoretical slope of 1 in all cases, implying that the number of operations in our multigrid solver increased approximately linearly with the number of computational nodes. This was not the case in the successive over-relaxation method, whose slope was 1.32 for a typical solidification simulation.

- [1] M. Haataja and F. Léonard, *Phys. Rev. B* **69**, 081201(R) (2004).
- [2] S. Y. Hu and L. Q. Chen, *Acta Mater.* **49**, 463 (2001).
- [3] D. Rodney, Y. L. Bouar, and A. Finel, *Acta Mater.* **51**, 17 (2003).
- [4] H. Van Swygenhoven, *Mater. Sci. Eng., A* **483–484**, 33 (2008).
- [5] V. Yamakov, D. Wolfz, and S. R. Phillpot, *Philos. Mag. Lett.* **83**, 385 (2003).
- [6] J. Schiøtz and K. W. Jacobsen, *Science* **301**, 1357 (2003).
- [7] M. Dao, L. Lu, K. Liu, H. Rosner, R. Asaro, J. D. Hosson, and E. Ma, *Acta Mater.* **55**, 4041 (2007).
- [8] K. R. Elder, M. Katakowski, M. Haataja, and M. Grant, *Phys. Rev. Lett.* **88**, 245701 (2002).
- [9] K. R. Elder and M. Grant, *Phys. Rev. E* **70**, 051605 (2004).
- [10] P. Stefanovic, M. Haataja, and N. Provatas, *Phys. Rev. Lett.* **96**, 225504 (2006).
- [11] K. R. Elder, N. Provatas, J. Berry, P. Stefanovic, and M. Grant, *Phys. Rev. B* **75**, 064107 (2007).
- [12] J. Berry, K. R. Elder, and M. Grant, *Phys. Rev. B* **77**, 224114 (2008); <http://link.aps.org/abstract/PRB/v77/e224114>
- [13] J. Berry, M. Grant, and K. R. Elder, *Phys. Rev. E* **73**, 031609 (2006); <http://link.aps.org/abstract/PRE/v73/e031609>
- [14] S. Majaniemi and M. Grant, *Phys. Rev. B* **75**, 054301 (2007).
- [15] S. Majaniemi, M. Nonomura, and M. Grant, *Eur. Phys. J. B* **66**, 329 (2008).
- [16] T. V. Ramakrishnan and M. Yussouff, *Phys. Rev. B* **19**, 2775 (1979).
- [17] N. Goldenfeld, B. P. Athreya, and J. A. Dantzig, *Phys. Rev. E* **72**, 020601(R) (2005).
- [18] K.-A. Wu and A. Karma, *Phys. Rev. B* **76**, 184107 (2007).
- [19] S. Majaniemi and N. Provatas, *Phys. Rev. E* **79**, 011607 (2009).
- [20] B. P. Athreya, N. Goldenfeld, J. A. Dantzig, M. G. Greenwood, and N. Provatas, *Phys. Rev. E* **76**, 056706 (2007).
- [21] E. Hall, *Proc. R. Soc. London Ser. B* **64**, 747 (1951).
- [22] N. Petch, *J. Iron Steel Inst., London* **174**, 25 (1953).
- [23] Y. Wang, *Scr. Mater.* **48**, 1581 (2003).
- [24] M. Haouaoui, I. Karaman, K. T. Hartwig, and H. Maier, *Metall. Mater. Trans. A* **35**, 2935 (2004).
- [25] F. Ebrahimi, Q. Zhai, and D. Kong, *Scr. Mater.* **39**, 315 (1998).
- [26] S. Ichikawa, K. Miyazawa, H. Ichinose, and K. Ito, *Nanostruct. Mater.* **11**, 1301 (1999).
- [27] A. Chokshi, A. Rosen, J. Karch, and H. Gleiter, *Scr. Metall.* **23**, 1679 (1989).
- [28] K. Lu, J. Wang, and D. Wei, *Scr. Metall. Mater.* **24**, 2319 (1990).
- [29] A. M. El-Sherik, U. Erb, G. Palumbo, and K. Aust, *Scr. Metall. Mater.* **27**, 1185 (1992).
- [30] R. Valiev, F. Chmelik, F. Bordeaux, G. Kapelski, and B. Baudelet, *Scr. Metall. Mater.* **27**, 855 (1992).
- [31] J. Chen, L. Lu, and K. Lu, *Scr. Mater.* **54**, 1913 (2006).
- [32] J. Weertman and J. R. Weertman, *Physical Metallurgy* (North-Holland, Amsterdam, 1965), Chap. 20, pp. 1332–1333.
- [33] G. Nieman, J. Weertman, and R. Siegel, *Scr. Metall. Mater.* **24**, 145 (1990).
- [34] J. Schiøtz, F. D. Di Tolla, and K. W. Jacobsen, *Nature (London)* **391**, 561 (1998).
- [35] H. Hahn, P. Mondal, and K. Padmanabhan, *Nanostruct. Mater.* **9**, 603 (1997).
- [36] D. Wolf, V. Yamakov, S. Phillpot, A. Mukherjee, and H. Gleiter, *Acta Mater.* **53**, 1 (2005).
- [37] M. Murayama, J. M. Howe, H. Hidaka, and S. Takaki, *Science* **295**, 2433 (2002); <http://www.jstor.org/stable/3076167>
- [38] K. Kumar, H. V. Swygenhoven, and S. Suresh, *Acta Mater.* **51**, 5743 (2003).
- [39] M. Zhao, J. Li, and Q. Jiang, *J. Alloys Compd.* **361**, 160 (2003).
- [40] W. Press, S. Teukolsky, W. Vetterling, and B. Flannery, *Numerical Recipes in Fortran 77* (Cambridge University Press, Cambridge, 1992).
- [41] U. Trottenberg, C. Oosterlee, and A. Schuller, *Multigrid* (Academic Press, London, 2001).
- [42] J. Kim, K. Kang, and J. Lowengrub, *J. Comput. Phys.* **193**, 511 (2004).